

The predicted compressive strength of a pyramidal lattice made from case hardened steel tubes

L. St-Pierre, N.A. Fleck* and V.S. Deshpande

Department of Engineering, University of Cambridge, Trumpington Street,
Cambridge, CP2 1PZ, UK

July 11, 2013

Abstract

A sandwich panel with a core made from solid pyramidal struts is a promising candidate for multifunctional application such as combined structural and heat-exchange function. This study explores the performance enhancement by making use of hollow struts, and examines the elevation in the plastic buckling strength by either strain hardening or case hardening. Finite element simulations are performed to quantify these enhancements. Also, the sensitivity of competing collapse modes to tube geometry and to the depth of case hardening is determined. A comparison with other lattice materials reveals that the pyramidal lattice made from case hardened steel tubes outperforms lattices made from solid struts of aluminium or titanium and has a comparable strength to a core made from carbon fibre reinforced polymers.

Keywords: *Lattice materials, Finite element analysis, Plastic buckling, Sandwich panels.*

* Corresponding author. Tel: +44 1223 748240 Fax: +44 1223 332662 Email: naf1@eng.cam.ac.uk

1 Introduction

In recent years, there has been significant research progress in the development of lightweight sandwich panels with lattice core topologies. Such sandwich panels are subjected to quasi-static service loads, or to dynamic loads associated with various threats such as water blast and sand blast in military applications. The strength of the core depends upon its topology, relative density and the mechanical properties of the parent solid, see Ashby (2006). Type 304 stainless steel is a promising core material, particularly for marine applications due to its high strain hardening capacity and its high corrosion resistance. Over the last decade, several core topologies have been manufactured from type 304 stainless steel, for example the corrugated core (Côté et al., 2006), square honeycomb core (Côté et al., 2004) and the pyramidal core made from solid struts (Zok et al., 2004) or hollow tubes (Queheillalt and Wadley, 2005, 2011). For each core topology, the measured compressive strength $\bar{\sigma}_{pk}$ is plotted in Fig. 1 as a function of relative density $\bar{\rho}$ (defined as the ratio of the density of the lattice core to that of the solid). The compressive strength is normalised by $\bar{\rho}\sigma_y$, where σ_y is the yield strength of the parent material. The results indicate that the hollow pyramidal core is stronger than other core topologies, particularly at low values of relative density.

The unit cell of a hollow pyramidal lattice is shown in Fig. 2; its geometry is defined by the inclination angle ω , the tube length l , the external diameter d and wall thickness t . Pingle et al. (2011a) used the finite element method to examine the influence of tube geometry upon the collapse mode of a hollow pyramidal lattice for the choice $\omega = 55^\circ$. Their results are presented in the form of a collapse mechanism

map¹ and this is reproduced in Fig. 3. Six collapse modes are identified, and the active mode depends upon the tube slenderness ratio l/d and the normalised wall thickness t/d . This map was developed for a hollow pyramidal lattice made from annealed type 304 stainless steel, of yield strength 180 MPa, and high strain hardening capacity. The stress versus strain response as used by Pingle et al. (2011a) is reproduced in Fig. 4.

In the first part of this study, the effect of strain hardening upon the collapse mode and compressive strength of a hollow pyramidal lattice will be evaluated. In the second part, the effect of surface carburisation will be investigated. A low temperature carburisation treatment has been developed recently for stainless steel and, depending on the duration of the treatment, carburisation depths of 25-70 μm can be achieved (Cao et al., 2003; Michal et al., 2006). The potential of carburisation to increase the strength of lattice materials made from stainless steel has not been investigated before; however, other surface treatments, such as plasma electrolytic oxidation and electrochemical anodizing, have been used recently to increase the compressive strength of aluminium metal foams (Abdulla et al., 2011; Bele et al., 2011; Dunleavy et al., 2011).

The effect of strain hardening and carburisation upon the compressive strength of a pyramidal lattice is studied below, with a focus on two vertical trajectories on the collapse mechanism map in Fig. 3: the left-hand trajectory, marked by a dashed line, represents tubes with a normalised wall thickness $t/d = 0.1$, whereas the right-hand

¹ Similar collapse mechanism maps were developed experimentally for vertical tubes made from aluminium alloy by Andrews et al. (1983) and Guillow et al. (2001). Maps can also be developed for other loading conditions; see for example Pingle et al. (2011b) for a map of the hollow pyramidal lattice under transverse shear.

trajectory denotes pyramidal lattices made from solid struts, $t/d = 0.5$. For both trajectories, the slenderness ratio l/d is varied from 1 to 100.

This paper is organised as follows. First, the geometry of the hollow pyramidal lattice is presented in Section 2. Second, the effect of strain hardening is addressed in Section 3 and the influence of carburisation is analysed in Section 4. Both Sections 3 and 4 include a comparison between the predicted compressive strength of tubes and of solid struts.

2 Geometry of the pyramidal lattice

The unit cell of a hollow pyramidal lattice is shown in Fig. 2a. Its geometry is defined by the tube length l , external diameter d , wall thickness t and inclination ω , as mentioned earlier. A top view of the lattice, see Fig. 2b, reveals that the tube centres are offset by a distance k from the centre of the pyramid. The distance k is constrained such that

$$k \geq k_{\min} = \frac{d\sqrt{1 + \sin^2 \omega}}{2 \sin \omega}, \quad (1)$$

and the limit $k = k_{\min}$ corresponds to the case where the tubes touch each other at the face-sheets. The relative density of the hollow pyramidal lattice is related to the core geometry via

$$\bar{\rho} = \frac{2\pi(d^2 - (d - 2t)^2)}{(4k + 2l \cos \omega)^2 \sin \omega} = \frac{2\pi \frac{t}{d} \left(1 - \frac{t}{d}\right)}{\left(2\alpha + \frac{l}{d} \cos \omega\right)^2 \sin \omega}, \quad (2)$$

$$\bar{\rho} = \frac{2\pi(d^2 - (d - 2t)^2)}{(4k + 2l \cos \omega)^2 \sin \omega} \quad \text{IS FINE. NO NEED FOR THE 2ND EXPRESSION}$$

where α is a function of inclination ω according to

$$\alpha \equiv \frac{\sqrt{1 + \sin^2 \omega}}{2 \sin \omega}. \quad (3)$$

We will limit our attention to the case where the tube ends touch, $k = k_{\min}$, and the inclination angle is $\omega = 55^\circ$. With these two parameters held fixed, Eq. (2) is used to plot contours of relative density $\bar{\rho}$ on the collapse mechanism map in Fig. 3. This collapse mechanism map was constructed by Pingle (2011a) for type 304 stainless steel tubes with axes of l/d and t/d . The limiting case of solid struts with $t/d = 0.5$ is also included in the map. The map was developed via Finite Element (FE) calculations in which the tubes were assumed to be made from an isotropic elastic-plastic J2 flow theory solid with a tensile stress versus strain curve reproduced in Fig. 4. Six collapse modes (A-F) were identified and the domains of dominance are shown in Fig. 3. The six collapse modes are exemplified in Fig. 3 by the deformed FE meshes of six geometries (a-f) marked by square symbols on the map.

3 Strengthening the pyramidal lattice by strain hardening

We proceed to explore the sensitivity of the collapse response of a pyramidal lattice to the degree of strain hardening. The parent material of the lattice was modelled as a rate-independent elastic-plastic solid in accordance with J2-flow theory. The elastic regime was linear and isotropic, as characterised by a Young's modulus $E = 200$ GPa and a Poisson's ratio $\nu = 0.3$. The yield strength of the material was set to $\sigma_Y^A = 200$ MPa. Two levels of strain hardening are compared: (i) $E_t = 0$, representing an elastic, ideally plastic solid and (ii) $E_t = 2$ GPa, a realistic value for stainless steel. The idealised stress versus strain curve with linear hardening is plotted in Fig. 4, and it is almost identical to the measured response of 304 stainless steel employed by Pingle et al. (2011a). A series of finite element simulations revealed that the collapse mechanism map, as derived by Pingle et al (2011a), remains valid for the modified

tensile response with linear hardening: there is a negligible shift in the boundaries of the map with the slight change in constitutive law.

3.1 Finite element modelling

All simulations were performed with the implicit solver of the commercially available finite element software Abaqus (version 6.10). The boundary conditions, mesh, geometric imperfections, material properties and dimensions are detailed below. The inclination was held fixed at $\omega = 55^\circ$ and two different cross-sections were considered: (i) a tube with $t/d = 0.1$ and (ii) a solid strut corresponding to $t/d = 0.5$. For these two values of t/d , the slenderness ratio l/d was varied from 1 to 100. When the hollow pyramidal lattice is compressed by a downward displacement δ , an axial force develops in each tube of the lattice, and this axial force has a vertical component P . The nominal compressive stress $\bar{\sigma}$ on the front face-sheet is

$$\bar{\sigma} = \frac{8P}{(4k + 2l \cos \omega)^2}, \quad (4)$$

and the corresponding nominal compressive strain in the core is

$$\bar{\varepsilon} = \frac{\delta}{l \sin \omega}. \quad (5)$$

It is sufficient to consider only one tube to capture the compressive response of the hollow pyramidal lattice. The tubes were meshed using three-dimensional hexahedral elements (C3D8R in Abaqus notation) with at least five elements through the wall

thickness. A small geometric imperfection was included in all simulations; it had the shape of the first buckling mode with an amplitude $\zeta = 0.05t$. The sensitivity of compressive response to the level of imperfection is reported in Appendix A. Therein it is shown that the effect of the imperfection quickly saturates: the response of an imperfect lattice is relatively insensitive to the shape and amplitude of the imperfection.

The boundary conditions are illustrated in Fig. 5. The front and back face-sheets were modelled as rigid surfaces and perfect bonding was assumed between the tube and face-sheets. The back face was clamped against translational and rotational displacements whereas the front face had a prescribed downward displacement δ , see Fig. 5. No lateral motion (in the x_1 and x_2 directions) and no rotation were allowed for the front face. A hard frictionless contact was defined between all surfaces of the model, allowing the lattice to densify at large values of nominal compressive strain $\bar{\varepsilon}$.

3.2 Results for the tubular pyramidal lattice

Consider the stainless steel tube with $t/d = 0.1$. The four selected geometries $l/d = 1, 3, 20$ and 100 collapse in mode A, D, E and F, respectively (see Fig. 3). Their compressive responses are plotted in Fig. 6 in terms of the nominal compressive stress $\bar{\sigma}$ (normalised by the relative density $\bar{\rho}$ and the yield strength σ_Y^d) versus the nominal compressive strain $\bar{\varepsilon}$. For each geometry, the compressive response is given for (i) $E_t = 0$ and (ii) $E_t = 2$ GPa. The deformed geometries corresponding to these responses are given in Table 1 to exemplify the four collapse modes of the tube. It is clear from the table that the collapse modes are qualitatively the same for the strongly work hardening solid and for the elastic, ideally plastic case. However, the deformed

geometries for the strain hardening solid ($E_t = 2$ GPa) reveal more diffuse plastic hinges than those obtained for an ideally plastic solid ($E_t = 0$).

All compressive responses shown in Fig. 6 exhibit a peak stress $\bar{\sigma}_{pk}$. The axial compressive stress in the tube reaches the yield strength when $\bar{\sigma}_{pk} / (\bar{\rho}\sigma_Y^A) = \sin^2 \omega \approx 0.67$ (Queheillalt and Wadley, 2005, 2011). Of the four collapse modes shown in Fig. 6, only elastic buckling (mode F) has a peak stress below the yield load. The influence of strain hardening varies from one mode to the next, as follows.

An axisymmetric bulge forms for $l/d = 1$ (mode A), see Fig. 6a. Strain hardening has a significant influence on the compressive response: the peak stress increases by a factor of three when E_t is increased from 0 to 2 GPa. Now consider the case $l/d = 3$. Collapse involves the formation of a two-lobe diamond (mode D), see Fig. 6b. The oscillations in response reflect the formation of the two lobes. Again, material strain hardening increases the peak stress, but the increase is slightly less than for the previous case $l/d = 1$. The tube with $l/d = 20$ undergoes global plastic buckling (mode E). For both choices of strain hardening, the axial compressive stress in the tube attains a peak value equal to the yield strength $\bar{\sigma}_{pk} / (\bar{\rho}\sigma_Y^A) \approx 0.67$, see Fig. 6c. The tube then buckles and forms a plastic hinge at mid-length. However, the post-peak response is stronger for $E_t = 2$ GPa than for $E_t = 0$. Finally, a tube with slenderness ratio $l/d = 100$ collapses by elastic buckling (mode F), see Fig. 6d. Strain hardening has no effect upon the peak stress and has only a minor effect upon the post-peak response. The stress drops sharply after the peak due to the development of a plastic hinge at mid-length.

3.3 Results for the pyramidal lattice with solid struts

The map in Fig. 3 indicates that the solid strut ($t/d = 0.5$) made from annealed 304 stainless steel collapses in three distinct modes (B, E and F) depending upon the slenderness ratio l/d . As marked in Fig. 3, one geometry was selected in each of the three collapse modes: $l/d = 3$ for mode B, $l/d = 20$ for mode E and $l/d = 100$ for mode F. The compressive responses of these three selected geometries are shown in Fig. 7. In each plot, results are given for $E_t = 0$ and $E_t = 2$ GPa. In addition, the deformed geometries corresponding to these compressive responses are shown in Table 2. The observed modes are independent of strain hardening, and are in agreement with the predictions in Fig. 3. Consider each slenderness ratio in turn.

A solid strut with $l/d = 3$ collapses by plastic barrelling (mode B) and its compressive response is particularly sensitive to strain hardening, see Fig. 7a. No peak value of stress exists, and we shall redefine $\bar{\sigma}_{pk}$ for this geometry as the stress at a nominal compressive strain $\bar{\epsilon} = 0.5$, following the convention of Pingle et al. (2011a). As the slenderness ratio of the solid strut is increased, the collapse mode switches to global plastic buckling (mode E), see Fig. 7b, and then to elastic buckling (mode F), see Fig. 7c. The influence of strain hardening upon the responses of these two collapse modes has already been discussed above for tubes, and the results for solid struts are similar: (i) the peak stress for $l/d = 20$ and 100 is insensitive to E_t and (ii) material strain hardening elevates the post-peak response when $l/d = 20$, but has minimal effect when $l/d = 100$.

The deformed geometries shown in Table 2 for solid struts confirm the observations already made for tubes: strain hardening results in more diffuse plastic hinges, but the collapse mode is insensitive to E_t . For both the tube and the solid strut, our simulations indicate that the collapse mechanism map shown in Fig. 3 is relatively

insensitive to the strain hardening modulus; we emphasise that we have chosen two extreme values of E_t in this study.

3.4 Comparison between the tubular and solid pyramidal lattices

A direct comparison of the strength of tubes ($t/d = 0.1$) and solid struts ($t/d = 0.5$) is given by plotting the normalised peak stress $\bar{\sigma}_{pk}/(\bar{\rho}\sigma_y^A)$ versus the relative density $\bar{\rho}$ in Fig. 8. Peak strengths (and the observed collapse modes) are given for both $E_t = 0$ and $E_t = 2$ GPa. Three regimes can be identified in Fig. 8.

1. Tubes with $\bar{\rho} < 0.0005$ and solid struts with $\bar{\rho} < 0.002$ collapse by elastic buckling (mode F). For this collapse mode, the normalised peak stress increases with increasing relative density. Since collapse is elastic in nature, the degree of strain hardening has no effect upon the peak stress.
2. When the relative density is in the range $0.0005 \leq \bar{\rho} \leq 0.01$ for the tubes, and in the range $0.002 \leq \bar{\rho} \leq 0.04$ for the solid struts, global plastic buckling (mode E) occurs. Again, the peak stress is insensitive to the level of strain hardening.
3. Finally, when $\bar{\rho} > 0.01$ for the tubes and $\bar{\rho} > 0.04$ for the solid struts, the magnitude of $\bar{\sigma}_{pk}/(\bar{\rho}\sigma_y^A)$ for $E_t = 2$ GPa exceeds that for $E_t = 0$. Note that the transition geometry $\bar{\rho} = 0.01$ for the tube, and $\bar{\rho} = 0.04$ for the solid strut, both correspond to a slenderness ratio $l/d \approx 10$, see Fig. 3 or refer to Eq. (2).

It is clear from Fig. 8 that the tube outperforms the solid strut for low values of relative density, $\bar{\rho} < 0.002$. This is because the transition from global plastic buckling (mode E) to elastic buckling (mode F) occurs at a lower value of relative density for the tube than for the solid strut. In contrast, at high values of relative

density, $\bar{\rho} > 0.1$, the solid strut collapses by plastic barrelling (mode B) and outperforms the tube, especially for $E_t = 2$ GPa.

4 Strengthening the pyramidal lattice by case hardening

A steel part can be surface-hardened to a prescribed depth h by the diffusion of carbon, see Fig. 9 for the case of (a) a carburised tube and (b) a carburised solid strut. Consequently, the carburisation depth h adds a third non-dimensional parameter to our analysis; the compressive strength of the pyramidal lattice is now governed by l/d , t/d and h/d (with the inclination angle fixed at $\omega = 55^\circ$).

4.1 Finite element modelling

The boundary conditions, the mesh details and the geometric imperfections used in this section were the same as those used previously, see Section 3.1. Both annealed and carburised stainless steels were modelled as rate-independent, elastic-plastic solids in accordance with J2-flow theory. The elastic branch is linear and isotropic, as characterised by a Young's modulus $E = 200$ GPa and a Poisson's ratio $\nu = 0.3$. The surface layer of carburised stainless steel was treated as elastic, ideally plastic ($E_t = 0$) with a yield strength $\sigma_y^C = 2$ GPa. This high yield strength was estimated from a hardness test reported by Michal et al. (2006). The underlying annealed stainless steel has a yield strength $\sigma_y^A = 200$ MPa and a linear strain hardening response with a tangent modulus $E_t = 2$ GPa. The uniaxial tensile responses of annealed and carburised stainless steels are compared in Fig. 10.

Again, the slenderness ratio l/d was varied from 1 to 100 for both the tube ($t/d = 0.1$) and the solid strut ($t/d = 0.5$). Four values of normalised carburisation depth were considered $h/d = 0, 0.02, 0.04$ and 0.05 . Note that for $h/d = 0.05$, the entire cross-section of the tube ($t/d = 0.1$) is carburised.

4.2 Results for the tubular pyramidal lattice

The influence of carburisation upon the compressive response of a tube with $t/d = 0.1$ is shown in Fig. 11 for the four selected geometries. For each geometry, the results are given for a non-carburised tube, $h/d = 0$, and for a tube with a normalised carburisation depth $h/d = 0.05$. The deformed geometries corresponding to these responses are given in Table 3.

Carburisation significantly increases the peak compressive stress $\bar{\sigma}_{pk}$ of stubby tubes with $l/d = 1$ and 3, see Fig. 11a and b, respectively. Note that both carburised tubes have the same peak stress $\bar{\sigma}_{pk} = 6.7\bar{\rho}\sigma_Y^A$. This value corresponds to the plastic collapse stress $\bar{\sigma}_{pl} = \bar{\rho}\sigma_Y^C \sin^2 \omega \approx 6.7\bar{\rho}\sigma_Y^A$, since $\sigma_Y^C = 10\sigma_Y^A$. Recall that the entire cross-section of the tube is carburised when $h/d = 0.05$. In addition, the peak stress occurs at a larger value of nominal compressive strain for non-carburised tubes than for carburised ones. Annealed stainless steel has a high value of tangent modulus $E_t = 2$ GPa and consequently the non-carburised tubes display a significant amount of plastic hardening before reaching the peak stress. On the other hand, carburised stainless steel is modelled as an elastic, ideally plastic solid: strain hardening is absent in the carburised tubes.

The non-carburised tube of slenderness ratio $l/d = 20$ collapses by global plastic buckling (mode E) at a peak stress $\bar{\sigma}_{pk} = 0.67\bar{\rho}\sigma_Y^A$, see Fig. 11c. Carburising this tube increases the peak stress to $\bar{\sigma}_{pk} = 5.7\bar{\rho}\sigma_Y^A$; the collapse mode is now elastic buckling, at a load below the plastic collapse load $\bar{\sigma}_{pl} = 6.7\bar{\rho}\sigma_Y^A$. Thus, carburisation increases the peak stress, but also changes the collapse mode from plastic to elastic buckling.

Tubes of high slenderness ratio ($l/d = 100$) collapse by elastic buckling, and for this mode, the peak stress is insensitive to the degree of carburisation, see Fig. 11d. Recall that the Young's modulus is the same for both annealed and carburised stainless steels. On the other hand, the carburised tube has a stronger post-peak response than the non-carburised one.

Finally, the deformed geometries of non-carburised tubes ($h/d = 0$) are compared to those of carburised tubes ($h/d = 0.05$) in Table 3. In general, carburisation has a relatively small effect upon the deformation mode.

4.3 Results for the pyramidal lattice with solid struts

The compressive response of a solid strut ($t/d = 0.5$) is shown in Fig. 12 for the three selected geometries. For each geometry, the response of a non-carburised strut, $h/d = 0$, is compared to that of a carburised strut with $h/d = 0.05$. For completeness, the deformed geometries corresponding to these responses are given in Table 4. In contrast to the case of the carburised tube as analysed in the previous section, the cross-section of the carburised strut with $h/d = 0.05$ has a surface layer of carburised stainless steel and an inner core of annealed stainless steel.

The compressive response of the stubby strut ($l/d = 3$) is shown in Fig. 12a. It collapses by plastic barrelling (mode B), and carburisation increases the yield stress of the lattice from $0.67 \bar{\rho} \sigma_y^A$ to approximately $1.8 \bar{\rho} \sigma_y^A$. However, the slope of the plastic hardening response, which is characteristic of plastic barrelling, is less for carburised struts than for non-carburised ones. This can be explained by the relative degree of strain hardening of the two phases.

Carburisation significantly increases the peak stress of the solid strut with $l/d = 20$, see Fig. 12b. The collapse mode of the carburised strut ($h/d = 0.05$) is classified as elastic buckling (mode F) because at $\bar{\sigma}_{pk}$ the axial compressive stress in the strut is below the yield strength of carburised stainless steel (but greater than the yield strength of annealed stainless steel). A similar change in collapse mechanism was observed in the previous section for a tube with the same slenderness ratio. The strut of high slenderness ratio ($l/d = 100$) collapses by elastic buckling (mode F), and the peak strength is independent of the degree of carburisation, see Fig. 12c. Nevertheless, the presence of carburisation strengthens the post-peak response.

The deformed geometries of non-carburised struts ($h/d = 0$) are compared to those of carburised struts ($h/d = 0.05$) in Table 4. It is clear from Table 4 that carburisation has only a small effect upon the collapse mode.

4.4 Comparison between the tubular and solid pyramidal lattices

The normalised peak stress $\bar{\sigma}_{pk}/(\bar{\rho}\sigma_Y^A)$, for both $t/d = 0.1$ and 0.5 , is plotted as a function of relative density in Fig. 13. The results are shown for four selected values of normalised carburisation depth h/d ranging from 0 to 0.05. In addition, the collapse modes are identified for both the tube and the solid strut. Note that the regimes of collapse mode are different for non-carburised ($h/d = 0$) and carburised ($h/d > 0$) lattices. Four regimes can be identified in Fig. 13:

1. Tubes with $\bar{\rho} < 0.0005$ and solid struts with $\bar{\rho} < 0.002$ both collapse by elastic buckling (mode F). It is clear from Fig. 13 that carburisation has no effect on the peak stress for this particular collapse mode.

2. When the relative density of the non-carburised tube is in the range $0.0005 \leq \bar{\rho} < 0.004$ and that of the non-carburised solid strut is in the range $0.002 \leq \bar{\rho} < 0.02$, global plastic buckling (mode E) occurs whereas the carburised lattices collapse by elastic buckling (mode F). Here, carburisation increases the peak stress of the lattice and this increase is more significant for the tube than for the strut.
3. For tubes with $\bar{\rho} \geq 0.004$ and for solid struts with $0.02 \leq \bar{\rho} < 0.1$, carburisation increases the peak strength of the lattice, but it has no effect on the collapse mode.
4. Finally, solid struts with $\bar{\rho} \geq 0.1$ collapse by plastic barrelling (mode B) and carburisation has a negligible effect on $\bar{\sigma}_{pk}$ for this particular collapse mode. Recall that the compressive response for plastic barrelling does not exhibit a peak stress, see Fig. 12a, and $\bar{\sigma}_{pk}$ is re-defined as the stress at $\bar{\varepsilon} = 0.5$. Based upon this definition, the normalised peak stress is insensitive to carburisation, but this result is dependent upon the definition of $\bar{\sigma}_{pk}$.

4.5 Position of carburised lattices on the strength-density chart

A material property chart allows us to position different materials on a figure where each axis is a material property (Ashby, 2010). A chart of strength versus density is presented in Fig. 14, where fully-dense materials such as metals, ceramics, composites and polymers are compared to foams and lattices. The results for lattices are based on experimental data, and include tetrahedral lattices made from aluminium (Al) (Kooistra et al., 2004), pyramidal lattices made from titanium (Ti) (Queheillalt and Wadley, 2009) and carbon fibre reinforced polymer (CRFP) (Finnegan et al., 2007), collinear lattices made from titanium matrix composite (TMC) (Moongkhamklang et al., 2010) and textile lattices made from titanium (Moongkhamklang and Wadley,

2010). For comparison purposes, the results of the finite element simulations for a tube ($t/d = 0.1$) with a normalised carburisation depth $h/d = 0.05$ are plotted in Fig. 14. Carburised stainless steel was assumed to have a density $\rho_s = 8000 \text{ kg/m}^3$, hence the density of a carburised stainless steel lattice is given by $\rho = \bar{\rho}\rho_s$.

The results indicate that carburised pyramidal lattices are stronger than their metallic counterparts made from aluminium or titanium. For densities below 0.1 Mg/m^3 , the carburised pyramidal lattices are positioned at the outer boundary of material space, and compete with the strongest pyramidal lattices made from carbon fibre reinforced polymer. Recall that the carburised stainless steel possesses a yield strength $\sigma_y^A = 2 \text{ GPa}$ in this study. If carburisation (or another heat treatment) was able to elevate the yield strength above 2 GPa , then this would expand the current material space.

5 Concluding remarks

The finite element method was used to simulate the compressive response of a pyramidal lattice made from tubes ($t/d = 0.1$) or solid struts ($t/d = 0.5$), both with an inclination angle $\omega = 55^\circ$. First, the effect of material strain hardening was examined by comparing the compressive response of a lattice made from stainless steel to that of a lattice made from an ideally plastic solid. Strain hardening was found to increase the compressive strength of lattices with a slenderness ratio $l/d < 10$, but had no effect upon the compressive strength of lattices with $l/d > 10$. Furthermore, strain hardening had a negligible effect upon the collapse mode of the pyramidal lattice. This holds true for lattices made from tubes and made from solid struts.

The effect of surface carburisation upon the compressive response of a pyramidal lattice was also explored. The slenderness ratio l/d at which the collapse mode changes from plastic to elastic buckling was less for carburised lattices than for their

non-carburised counterparts. Carburisation also increased the peak strength of the lattice, except for geometries that collapse by elastic buckling. This increase in peak strength was more significant for a lattice made from tubes than for one made from solid struts. Finally, the performance of the pyramidal lattice made from carburised tubes was compared to other engineering materials and lattices on a chart of strength versus density. The carburised lattice is stronger than other metallic lattices made from aluminium or titanium and offers similar performance to pyramidal lattices made from carbon fibre reinforced polymers. The simulations presented in this paper suggest that surface carburisation can significantly enhance the strength of lattice materials, and this combination has the potential to expand the current material space. However, the embrittlement that accompanies carburisation was neglected in the simulations, and future experimental work should validate if this has a significant influence on the predictions reported above.

Acknowledgments

This research was sponsored by DARPA as part of a Multidisciplinary University Research Initiative on “A micro-cellular solids approach to thermo structural materials”. The authors are also grateful for the financial support of the Materials innovation institute M2i (project number MC2.06261) and of the Fonds Québécois de la Recherche sur la Nature et les Technologies (FQRNT).

References

Abdulla, T., Yerokhin, A., Goodall, R., 2011. Effect of plasma electrolytic oxidation coating on the specific strength of open-cell aluminium foams. *Mater. Des.* 32, 3742–3749.

Andrews, K.R.F., England, G.L., Ghani, E., 1983. Classification of the axial collapse of cylindrical tubes under quasi-static loading. *Int. J. Mech. Sci.* 25, 687-696.

Ashby, M.F., 2006. The properties of foams and lattices. *Philos. T. Roy. Soc. A* 364, 15-30.

Ashby, M.F., 2010. *Material selection in mechanical design*, fourth ed. Butterworth-Heinemann, Oxford.

Bele, E., Bouwhuis, B.A., Codd, C., Hibbard, G.D., 2011. Structural ceramic coatings in composite microtruss cellular materials. *Acta Mater.* 59, 6145–6154.

Cao, Y., Ernst, F., Michal, G.M., 2003. Colossal carbon supersaturation in austenitic stainless steels carburized at low temperature. *Acta Mater.* 51, 4171–4181.

Côté, F., Deshpande, V.S., Fleck, N.A., Evans, A.G., 2004. The out-of-plane compressive behavior of metallic honeycombs. *Mat. Sci. Eng. A* 380, 272-280.

Côté, F., Deshpande, V.S., Fleck, N.A., Evans, A.G., 2006. The compressive and shear responses of corrugated and diamond lattice materials. *Int. J. Solids Struct.* 43, 6220-6242.

Dunleavy, C.S., Curran, J.A., Clyne, T.W., 2011. Plasma electrolytic oxidation of aluminium networks to form a metal-cored ceramic composite hybrid material. *Compos. Sci. Technol.* 71, 908–915.

Finnegan, K., Kooistra, G., Wadley, H.N.G., Deshpande, V.S., 2007. The compressive response of carbon fiber composite pyramidal truss sandwich cores. *Int. J. Mater. Res.* 98, 1264–1272.

Guillow, S.R., Lu, G., Grzebieta, R.H., 2001. Quasi-static axial compression of thin-walled circular aluminium tubes, *Int. J. Mech. Sci.* 43, 2103-2123.

Kooistra, G.W., Deshpande, V.S., Wadley, H.N.G., 2004. Compressive behavior of age hardenable tetrahedral lattice truss structures made from aluminium. *Acta Mater.* 52, 4229–4237.

Michal, G.M., Ernst, F., Kahn, H., Cao, Y., Oba, F., Agarwal, N., Heuer, A.H., 2006. Carbon supersaturation due to paraequilibrium carburization: Stainless steels with greatly improved mechanical properties. *Acta Mater.* 54, 1597-1606.

Moongkhamklang, P., Deshpande, V.S., Wadley, H.N.G., 2010. The compressive and shear response of titanium matrix composite lattice structures. *Acta Mater.* 58, 2822–2835.

Moongkhamklang, P., Wadley, H.N.G., 2010. Titanium alloy lattice structures with millimeter scale cell sizes. *Adv. Eng. Mater.* 12, 1111–1116.

Pingle, S.M., Fleck, N.A., Deshpande, V.S., Wadley, H.N.G., 2011a. Collapse mechanism maps for a hollow pyramidal lattice. *Proc. R. Soc. A* 467, 985-1011.

Pingle, S.M., Fleck, N.A., Deshpande, V.S., Wadley, H.N.G., 2011b. Collapse mechanism maps for the hollow pyramidal core of a sandwich panel under transverse shear. *Int. J. Solids Struct.* 48, 3417-3430.

Queheillalt, D.T., Wadley, H.N.G., 2005. Pyramidal lattice truss structures with hollow trusses. *Mater. Sci. Eng. A* 397, 132-137.

Queheillalt, D.T., Wadley, H.N.G., 2009. Titanium alloy lattice truss structures. *Mater. Des.* 30, 1966–1975.

Queheillalt, D.T., Wadley, H.N.G., 2011. Hollow pyramidal lattice truss structures. *Int. J. Mater. Res.* 4, 389-400.

Zok, F.W., Waltner, S.A., Wei, Z., Rathbun, H.J., McMeeking, R.M., Evans, A.G., 2004. A protocol for characterizing the structural performance of metallic sandwich panels: application to pyramidal truss cores. *Int. J. Solids Struct.* 41, 6249-6271.

A. Influence of geometric imperfections

The sensitivity of the compressive response to the amplitude and shape of a geometric imperfection is explored in this appendix. The imperfection consists of one or multiple elastic buckling modes. The effect of the number of superimposed modes and the effect of amplitude is addressed below. The simulations were done for a tube $t/d = 0.1$ made from annealed stainless steel ($\sigma_Y^A = 200$ MPa and $E_t = 2$ GPa).

A.1 Influence of the number of superimposed modes

The effect of the number of superimposed elastic eigenmodes upon the compressive response of a tube with $t/d = 0.1$ is shown in Fig. A.1 for selected values of slenderness ratio l/d . In each plot, three cases are compared: (i) a perfect structure (no imperfection), (ii) an imperfection of amplitude $\zeta = 0.05t$ in the form of the first buckling mode and (iii) an imperfection of amplitude $\zeta = 0.05t$ in the form of the first four buckling modes superimposed². Except for the case of $l/d = 1$, the compressive response of the tube is imperfection sensitive; case (i) differs from cases (ii) and (iii). However, the results indicate that the compressive response of an imperfect tube is relatively insensitive to the number of modes superimposed: the responses for cases (ii) and (iii) are similar. Hence, an imperfection in the form of the first buckling mode is assumed in the body of the paper.

A.2 Influence of amplitude

The effect of imperfection amplitude upon the compressive response of a tube with $t/d = 0.1$ is shown in Fig. A.2 for selected values of l/d . In each plot, results are given for a perfect structure (no imperfection) and for an imperfection in the form of the first buckling mode with three different amplitudes $\zeta = 0.01t$, $0.05t$ and $0.1t$. Except for the case of $l/d = 3$, the compressive response is relatively insensitive to the

² Each eigenmode is ascribed the same amplitude.

imperfection amplitude in the range $\zeta = 0.01t - 0.1t$. Consequently, an imperfection amplitude $\zeta = 0.05t$ was used in all simulations.

A.3 Influence of imperfection upon the deformed geometry

The effect of a geometric imperfection upon the deformed geometry of a tube with $t/d = 0.1$ is shown in Table A.1 for selected values of l/d . Results are shown for a perfect structure (no imperfection) and for simulations with an imperfection in the form of the first buckling mode with an amplitude $\zeta = 0.05t$. For $l/d = 1$, the deformed geometries are imperfection insensitive but more slender tubes are, however, imperfection-sensitive in their collapse mode.

Figure captions

Fig. 1. The measured normalised compressive strength as a function of relative density for four different lattice core topologies made from type 304 stainless steel. Data taken from Côté et al. (2004, 2006), Queheillalt and Wadley (2011) and Zok et al. (2004).

Fig. 2. (a) Unit cell of the hollow pyramidal lattice. (b) Top view of the lattice.

Fig. 3. Collapse mechanism map for a hollow pyramidal lattice made from type 304 stainless steel. There are six collapse modes (A-F) exemplified by the six selected geometries (a-f) that are marked on the map using square symbols. The representative geometries considered in this study are indicated by circular symbols. Adapted from Pingle et al. (2011a).

Fig. 4. Uniaxial tensile responses of the two material models employed in the finite element simulations to analyse the influence of strain hardening. The measured response of type 304 stainless steel, which was employed in the simulations of Pingle et al. (2011a), is also included for comparison.

Fig. 5. Sketch of the finite element model used to simulate the compressive response of the hollow pyramidal lattice.

Fig. 6. Influence of the strain hardening modulus E_t upon the compressive response of a pyramidal lattice made from tubes $t/d = 0.1$. Results are given for (a) $l/d = 1$, (b) $l/d = 3$, (c) $l/d = 20$ (d) $l/d = 100$.

Fig. 7. Influence of the strain hardening modulus E_t upon the compressive response a pyramidal lattice made from solid struts $t/d = 0.5$. Results are given for (a) $l/d = 3$, (b) $l/d = 20$ and (c) $l/d = 100$.

Fig. 8. Influence of the strain hardening modulus E_t upon the normalised compressive strength of a pyramidal lattice made from tubes $t/d = 0.1$ or solid struts $t/d = 0.5$.

Fig. 9. Cross-sections of a carburised (a) tube and (b) solid strut. Both are shown for a normalised carburisation depth $h/d = 0.02$.

Fig. 10. Uniaxial tensile responses of annealed and carburised stainless steels. These material models were employed in the finite element simulations to analyse the influence of carburisation.

Fig. 11. Influence of the carburisation depth h/d upon the compressive response of a pyramidal lattice made from tubes $t/d = 0.1$. Results are given for (a) $l/d = 1$, (b) $l/d = 3$, (c) $l/d = 20$ (d) $l/d = 100$.

Fig. 12. Influence of the carburisation depth h/d upon the compressive response a pyramidal lattice made from solid struts $t/d = 0.5$. Results are given for (a) $l/d = 3$, (b) $l/d = 20$ and (c) $l/d = 100$.

Fig. 13. Influence of the carburisation depth h/d upon the normalised compressive strength of a pyramidal lattice made from tubes $t/d = 0.1$ or solid struts $t/d = 0.5$.

Fig. 14. Material property chart of compressive strength versus density. The predicted compressive strength of a pyramidal lattice made from carburised tubes (t/d

$= 0.1$ and $h/d = 0.05$) is also included. Al, aluminium; CRFP, carbon fibre reinforced polymers; Ti, titanium; TMC, titanium matrix composites.

Fig. A.1. Influence of imperfection shape upon the compressive response of a pyramidal lattice made from tubes $t/d = 0.1$. In all cases, the imperfection amplitude is $\zeta = 0.05t$. Results are given for (a) $l/d = 1$, (b) $l/d = 3$, (c) $l/d = 20$ (d) $l/d = 100$.

Fig. A.2. Influence of imperfection amplitude upon the compressive response of a pyramidal lattice made from tubes $t/d = 0.1$. In all cases, the imperfection shape is in the form of the first buckling mode. Results are given for (a) $l/d = 1$, (b) $l/d = 3$, (c) $l/d = 20$ (d) $l/d = 100$.

Table captions

Table 1. Influence of the strain hardening modulus E_t upon the deformed geometries of a pyramidal lattice made from tubes $t/d = 0.1$. Results are given for four selected values of l/d .

Table 2. Influence of the strain hardening modulus E_t upon the deformed geometries of a pyramidal lattice made from solid struts $t/d = 0.5$. Results are given for three selected values of l/d .

Table 3. Influence of the carburisation depth h/d upon the deformed geometries of a pyramidal lattice made from tubes $t/d = 0.1$. Results are given for four selected values of l/d .

Table 4. Influence of the carburisation depth h/d upon the deformed geometries of a pyramidal lattice made from solid struts $t/d = 0.5$. Results are given for three selected values of l/d .

Table A.1. Influence of a geometric imperfection upon the deformed geometries of a pyramidal lattice made from tubes $t/d = 0.1$. Results are given for four selected values of l/d .

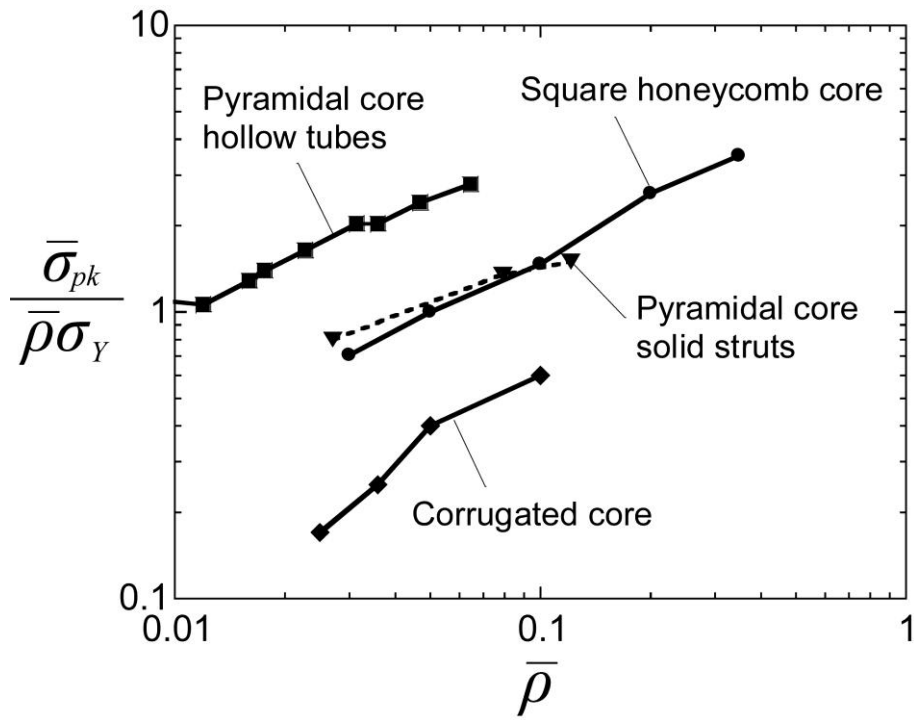


Fig. 1. The measured normalised compressive strength as a function of relative density for four different lattice core topologies made from type 304 stainless steel. Data taken from Côté et al. (2004, 2006), Queheillalt and Wadley (2011) and Zok et al. (2004).

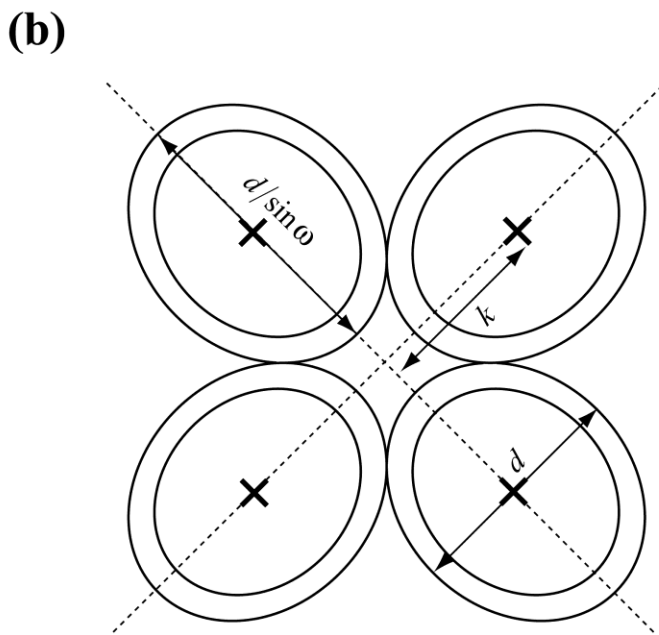
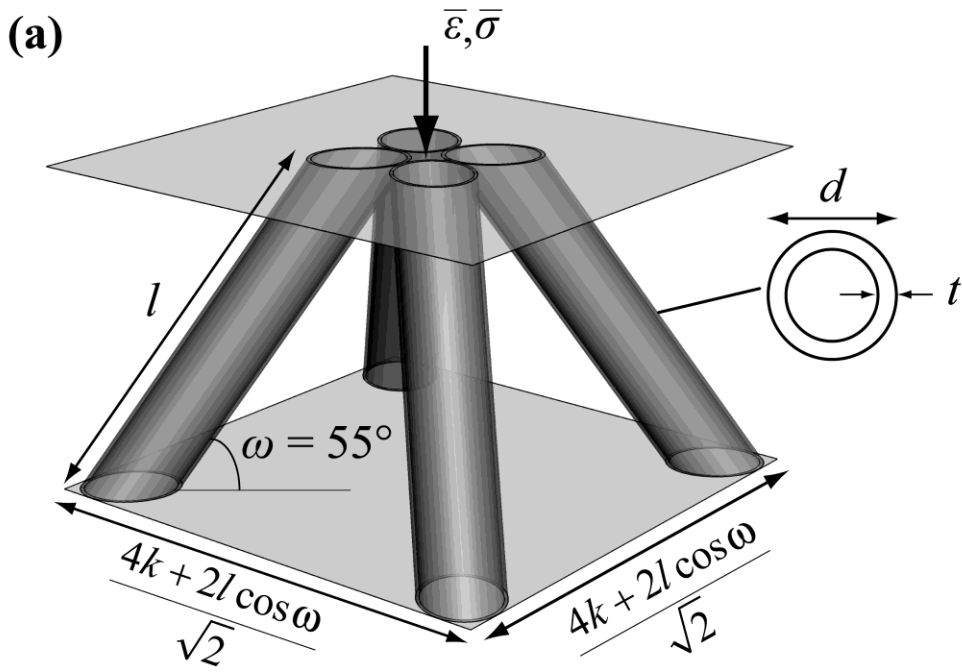
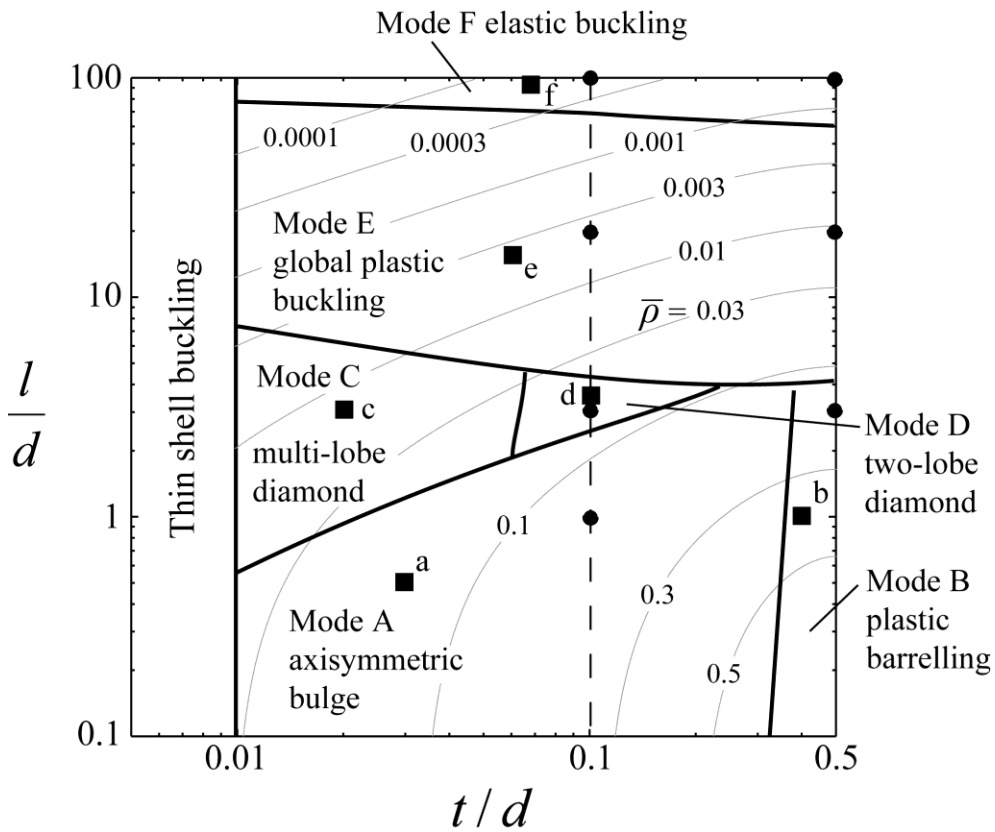


Fig. 2. (a) Unit cell of the hollow pyramidal lattice. (b) Top view of the lattice.

Collapse mechanism map



Collapse modes

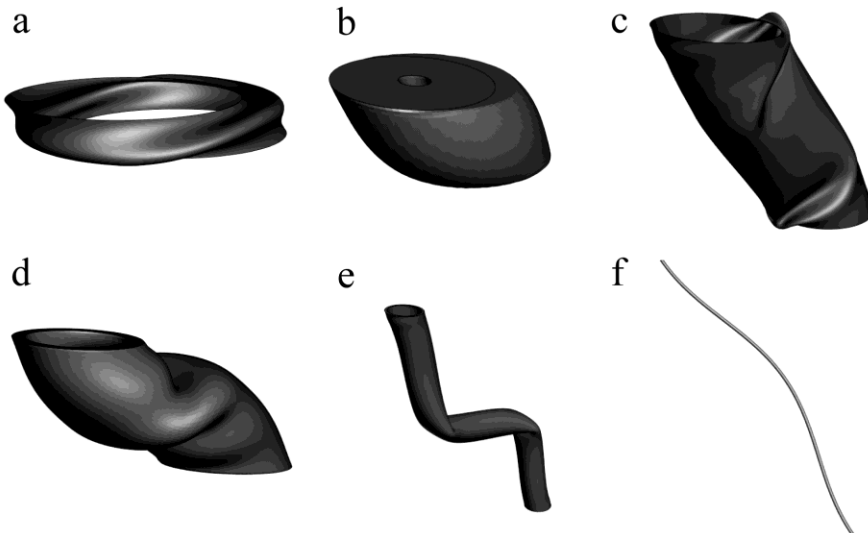


Fig. 3. Collapse mechanism map for a hollow pyramidal lattice made from type 304 stainless steel. There are six collapse modes (A-F) exemplified by the six selected geometries (a-f) that are marked on the map using square symbols. The representative geometries considered in this study are indicated by circular symbols. Adapted from Pingle et al. (2011a).

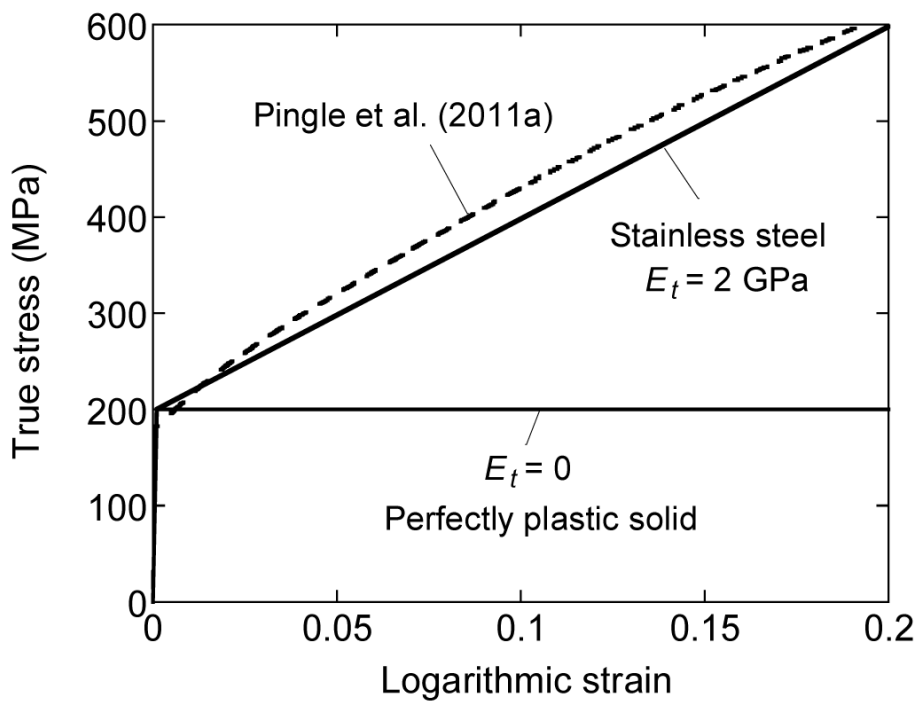


Fig. 4. Uniaxial tensile responses of the two material models employed in the finite element simulations to analyse the influence of strain hardening. The measured response of type 304 stainless steel, which was employed in the simulations of Pingle et al. (2011a), is also included for comparison.

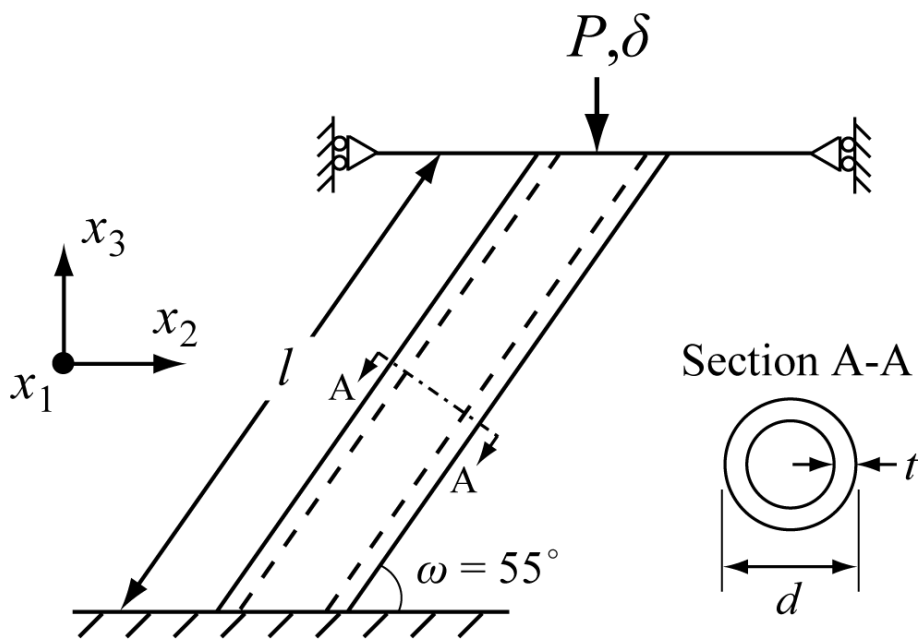


Fig. 5. Sketch of the finite element model used to simulate the compressive response of the hollow pyramidal lattice.

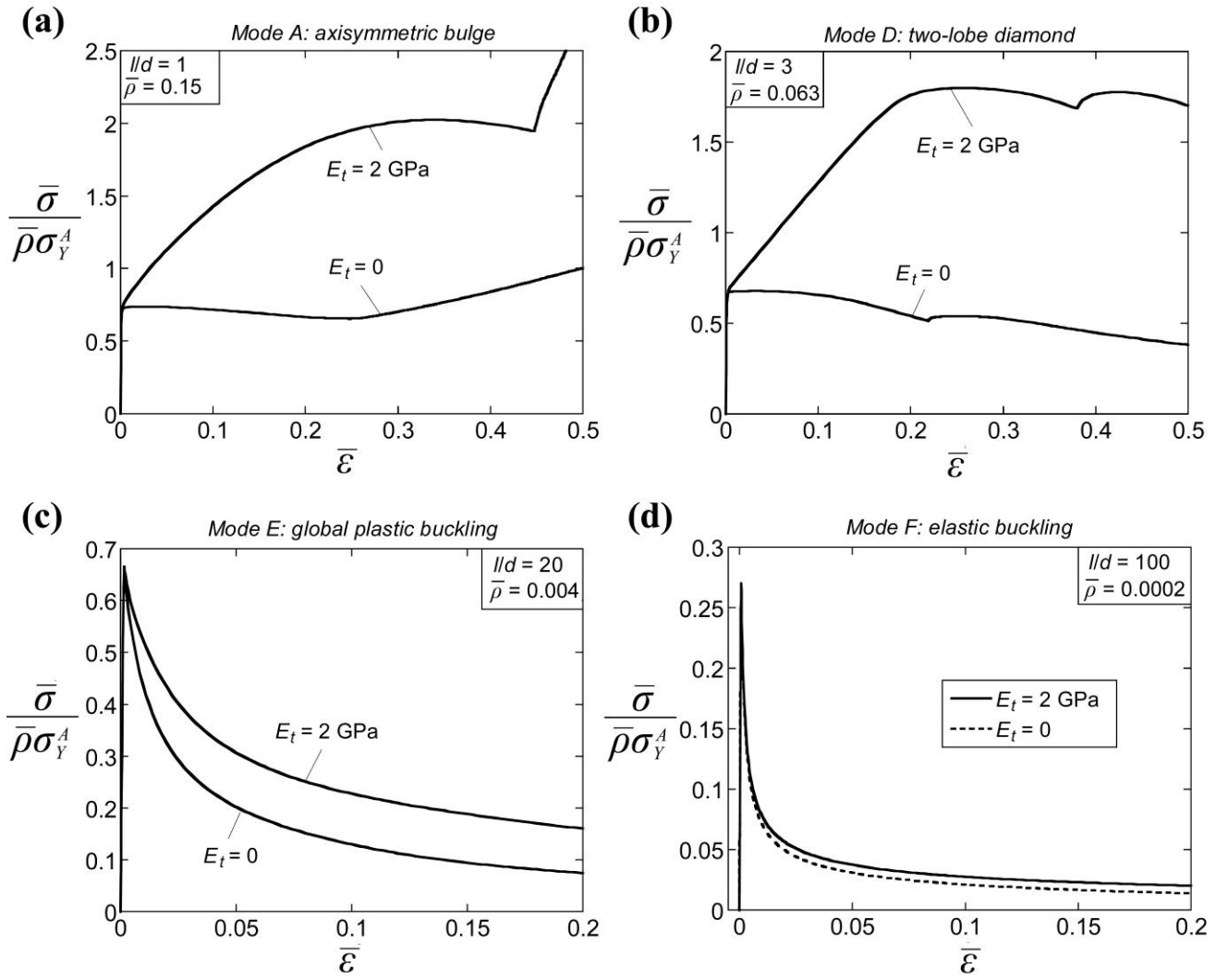


Fig. 6. Influence of the strain hardening modulus E_t upon the compressive response of a pyramidal lattice made from tubes $t/d = 0.1$. Results are given for (a) $l/d = 1$, (b) $l/d = 3$, (c) $l/d = 20$ (d) $l/d = 100$.

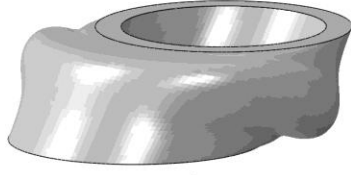
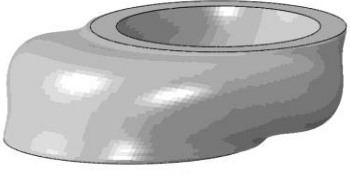
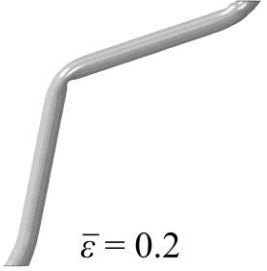
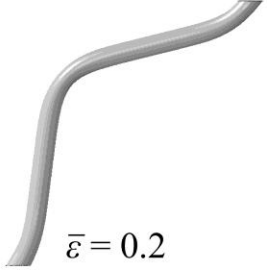
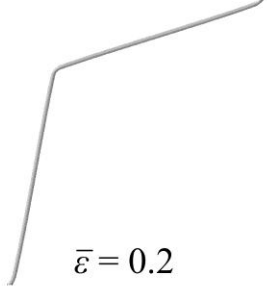
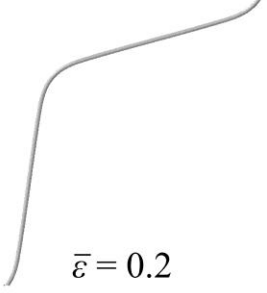
Geometry	$E_t = 0$	$E_t = 2 \text{ GPa}$
Mode A $l/d = 1$ $\bar{\rho} = 0.15$	 $\bar{\varepsilon} = 0.5$	 $\bar{\varepsilon} = 0.5$
Mode D $l/d = 3$ $\bar{\rho} = 0.064$	 $\bar{\varepsilon} = 0.5$	 $\bar{\varepsilon} = 0.5$
Mode E $l/d = 20$ $\bar{\rho} = 0.004$	 $\bar{\varepsilon} = 0.2$	 $\bar{\varepsilon} = 0.2$
Mode F $l/d = 100$ $\bar{\rho} = 0.0002$	 $\bar{\varepsilon} = 0.2$	 $\bar{\varepsilon} = 0.2$

Table 1. Influence of the strain hardening modulus E_t upon the deformed geometries of a pyramidal lattice made from tubes $t/d = 0.1$. Results are given for four selected values of l/d .

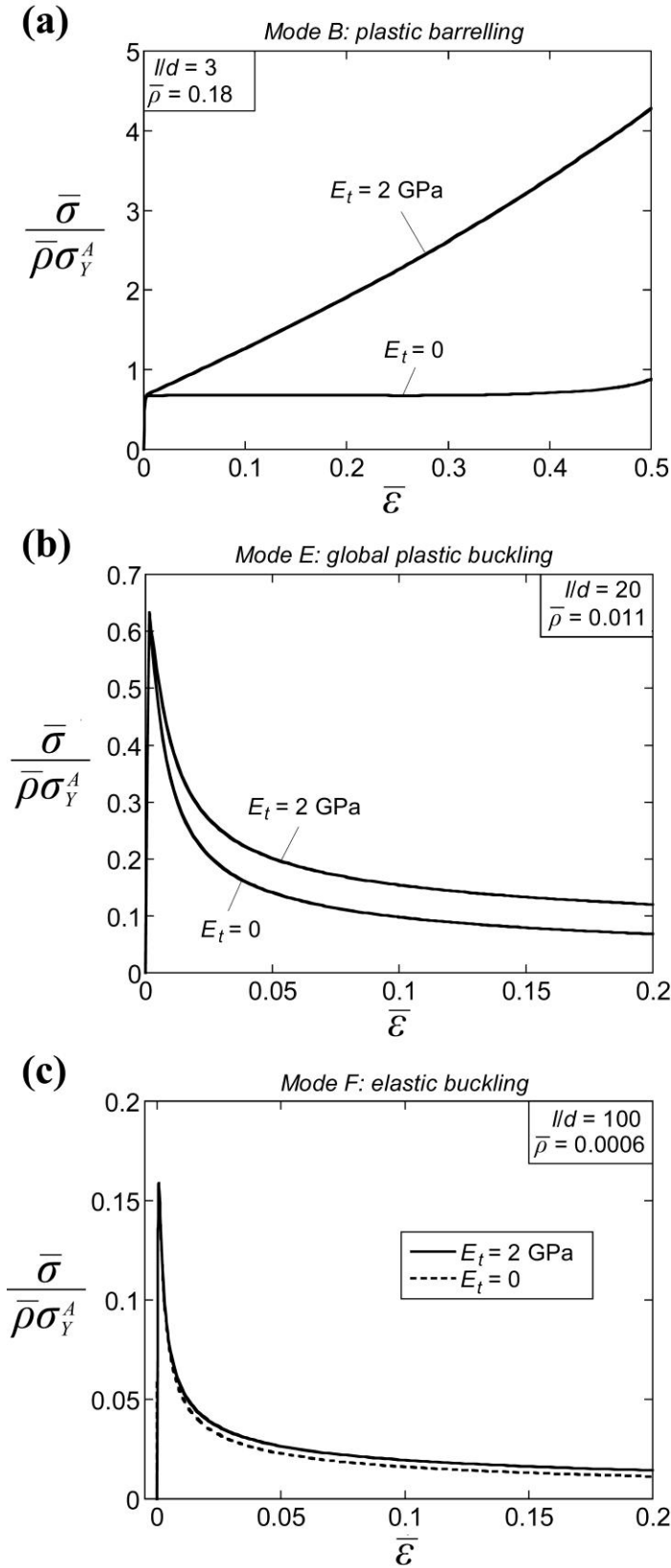


Fig. 7. Influence of the strain hardening modulus E_t upon the compressive response a pyramidal lattice made from solid struts $t/d = 0.5$. Results are given for (a) $l/d = 3$, (b) $l/d = 20$ and (c) $l/d = 100$.

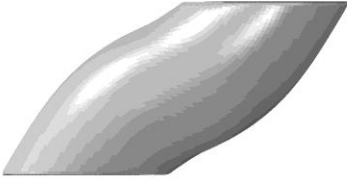
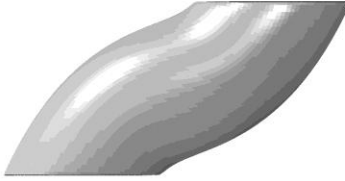
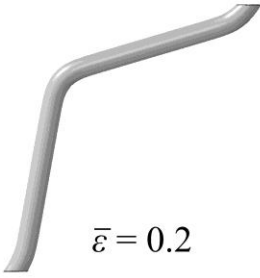
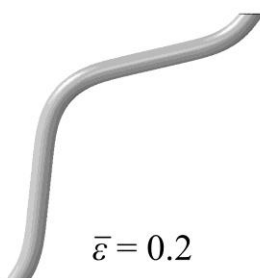
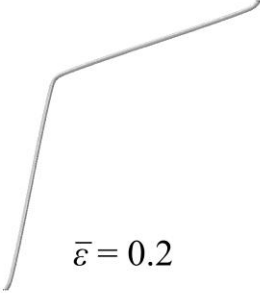
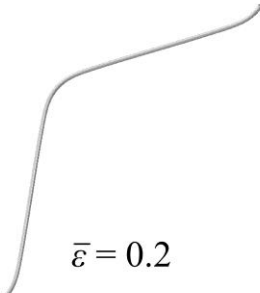
Geometry	$E_t = 0$	$E_t = 2 \text{ GPa}$
Mode B $l/d = 3$ $\bar{\rho} = 0.18$	 $\bar{\varepsilon} = 0.4$	 $\bar{\varepsilon} = 0.4$
Mode E $l/d = 20$ $\bar{\rho} = 0.011$	 $\bar{\varepsilon} = 0.2$	 $\bar{\varepsilon} = 0.2$
Mode F $l/d = 100$ $\bar{\rho} = 0.0006$	 $\bar{\varepsilon} = 0.2$	 $\bar{\varepsilon} = 0.2$

Table 2. Influence of the strain hardening modulus E_t upon the deformed geometries of a pyramidal lattice made from solid struts $t/d = 0.5$. Results are given for three selected values of l/d .

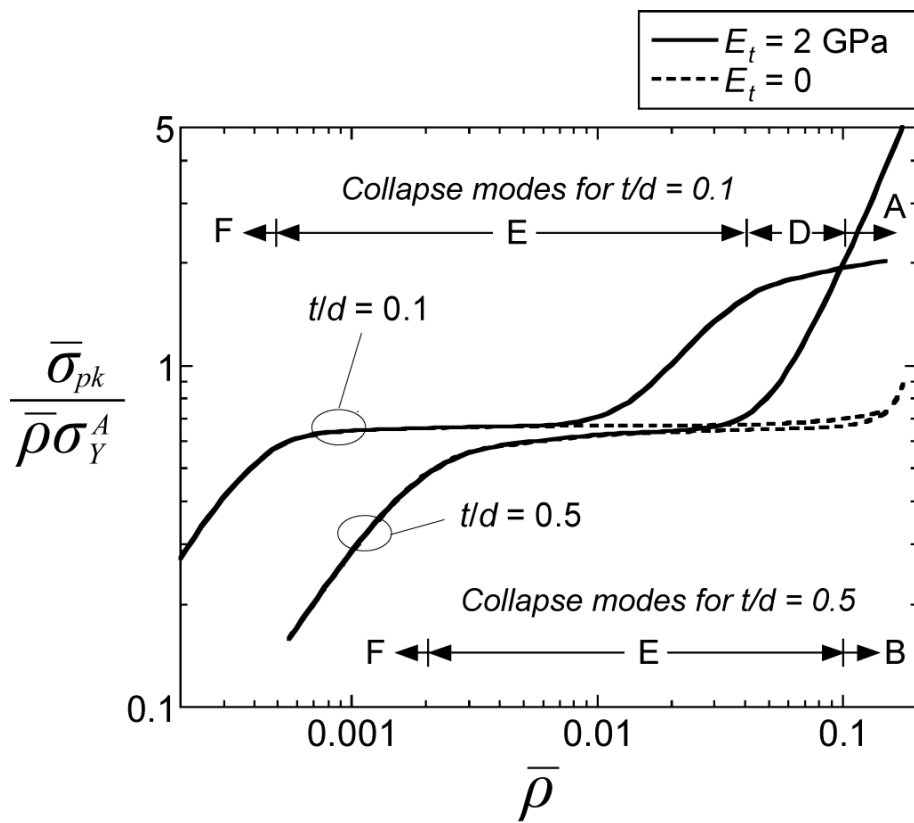


Fig. 8. Influence of the strain hardening modulus E_t upon the normalised compressive strength of a pyramidal lattice made from tubes $t/d = 0.1$ or solid struts $t/d = 0.5$.

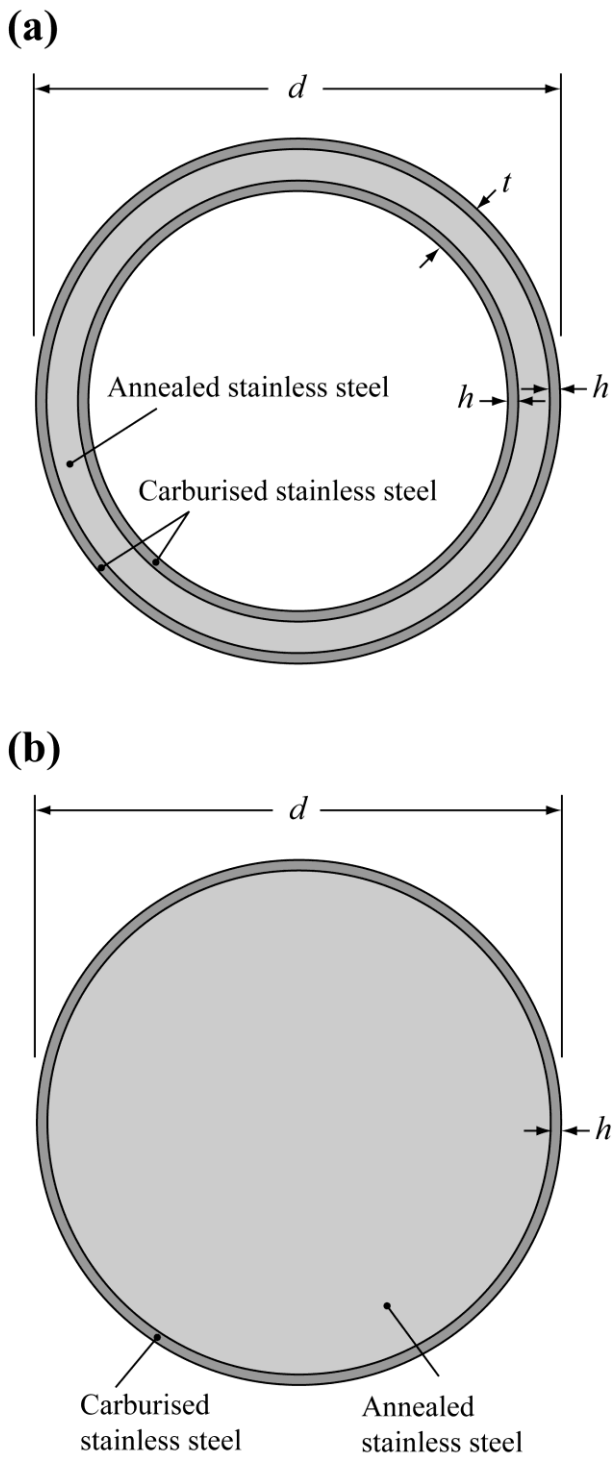


Fig. 9. Cross-sections of a carburised (a) tube and (b) solid strut. Both are shown for a normalised carburisation depth $h/d = 0.02$.

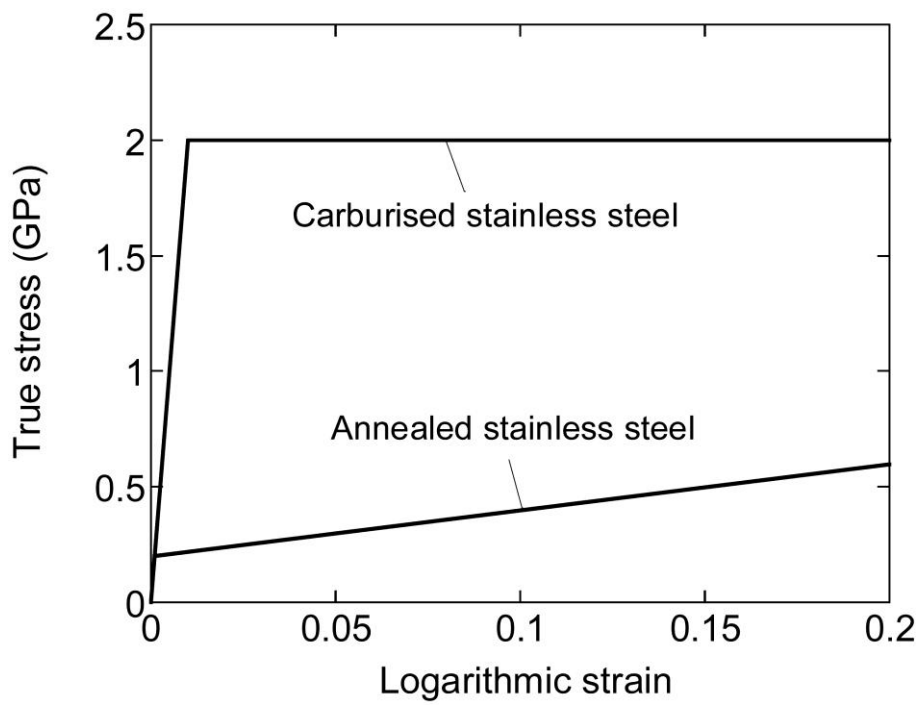


Fig. 10. Uniaxial tensile responses of annealed and carburised stainless steels. These material models were employed in the finite element simulations to analyse the influence of carburisation.

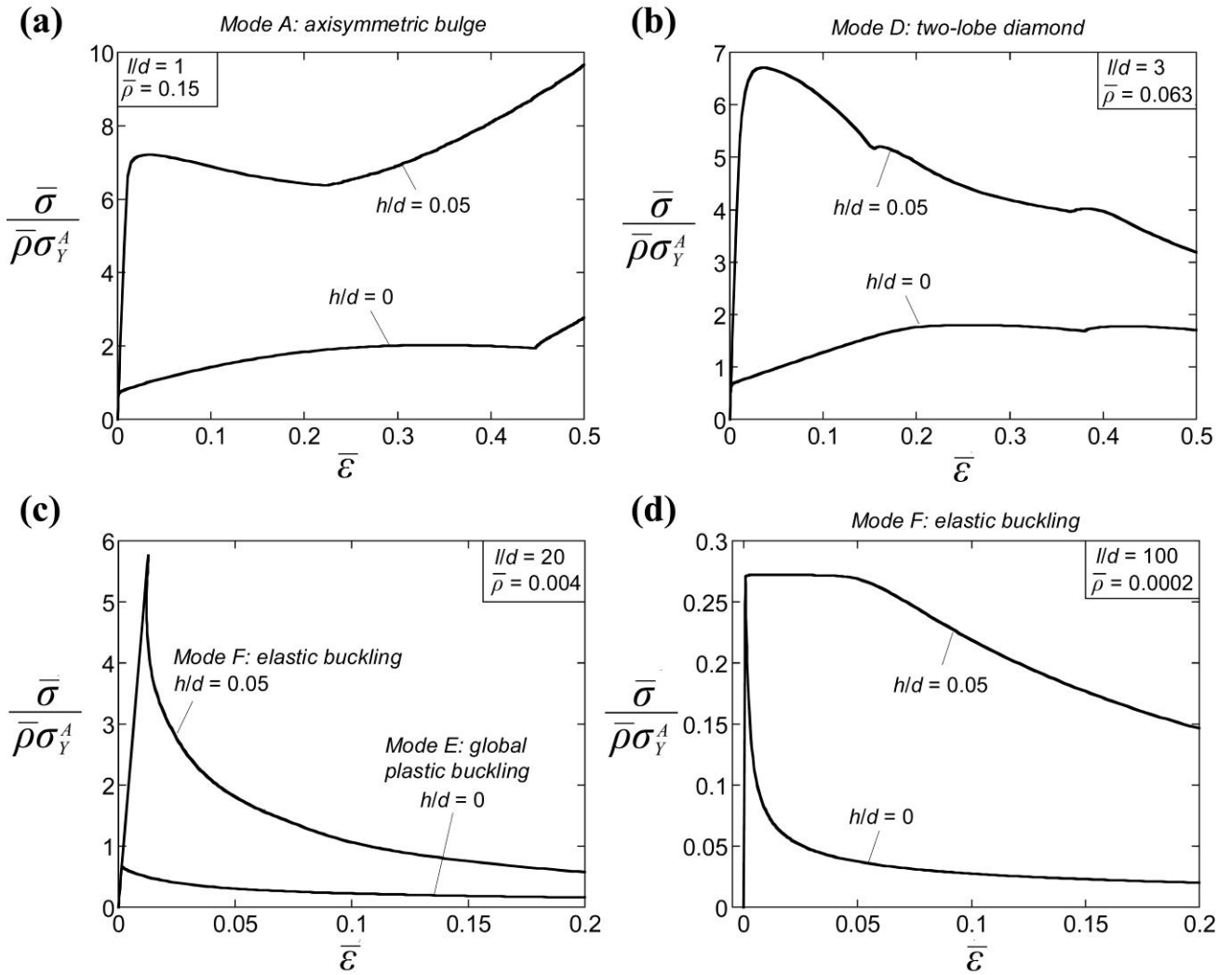


Fig. 11. Influence of the carburisation depth h/d upon the compressive response of a pyramidal lattice made from tubes $t/d = 0.1$. Results are given for (a) $l/d = 1$, (b) $l/d = 3$, (c) $l/d = 20$ (d) $l/d = 100$.

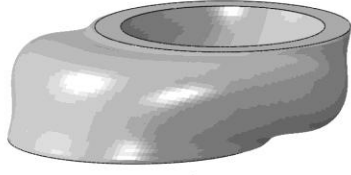
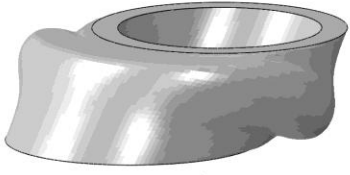
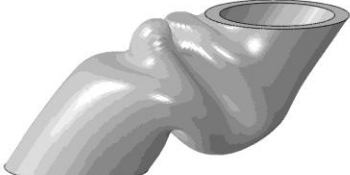
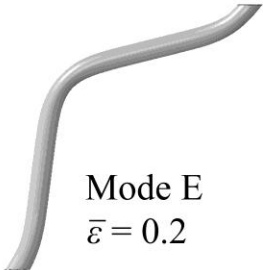
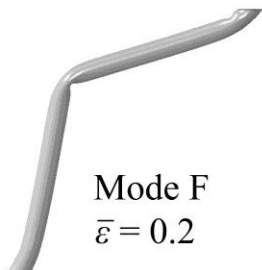
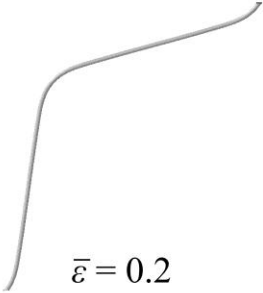
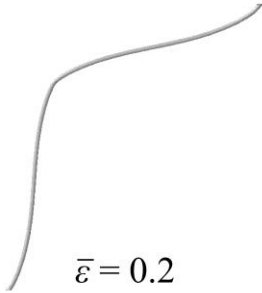
Geometry	$h/d = 0$	$h/d = 0.05$
Mode A $l/d = 1$ $\bar{\rho} = 0.15$	 $\bar{\varepsilon} = 0.5$	 $\bar{\varepsilon} = 0.5$
Mode D $l/d = 3$ $\bar{\rho} = 0.063$	 $\bar{\varepsilon} = 0.5$	 $\bar{\varepsilon} = 0.5$
$l/d = 20$ $\bar{\rho} = 0.004$	Mode E $\bar{\varepsilon} = 0.2$ 	Mode F $\bar{\varepsilon} = 0.2$ 
Mode F $l/d = 100$ $\bar{\rho} = 0.0002$	$\bar{\varepsilon} = 0.2$ 	$\bar{\varepsilon} = 0.2$ 

Table 3. Influence of the carburisation depth h/d upon the deformed geometries of a pyramidal lattice made from tubes $t/d = 0.1$. Results are given for four selected values of l/d .

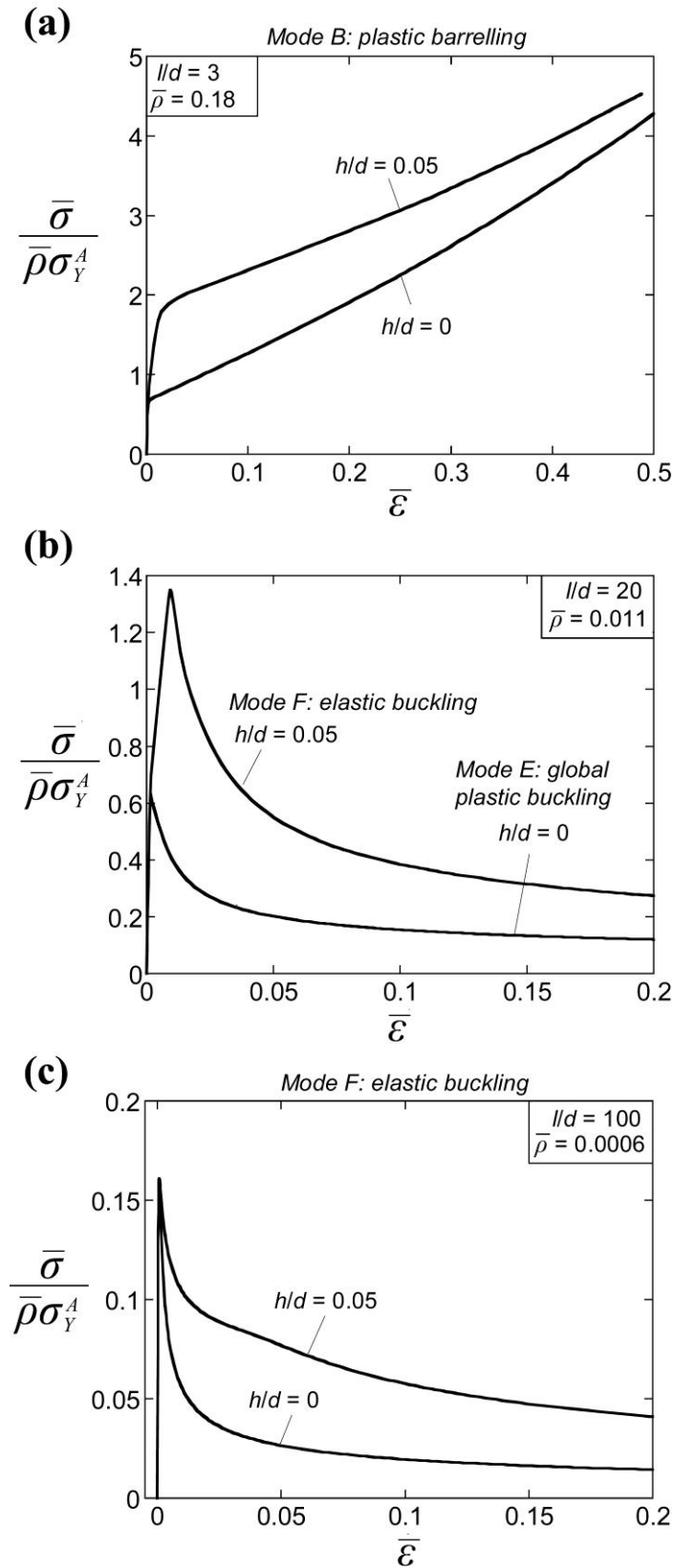


Fig. 12. Influence of the carburisation depth h/d upon the compressive response a pyramidal lattice made from solid struts $t/d = 0.5$. Results are given for (a) $l/d = 3$, (b) $l/d = 20$ and (c) $l/d = 100$.

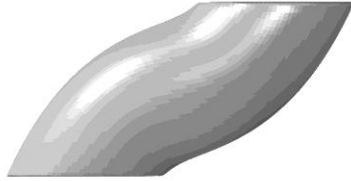
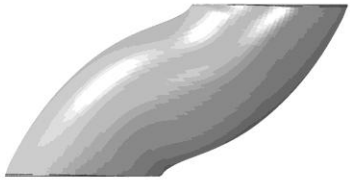
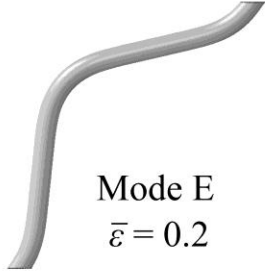
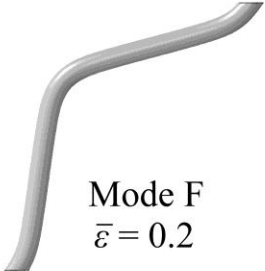
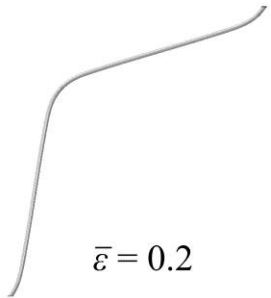
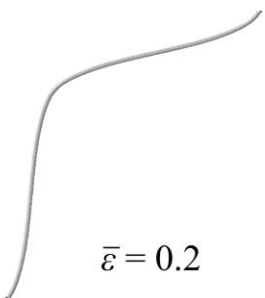
Geometry	$h/d = 0$	$h/d = 0.05$
Mode B $l/d = 3$ $\bar{\rho} = 0.18$	 $\bar{\varepsilon} = 0.4$	 $\bar{\varepsilon} = 0.4$
$l/d = 20$ $\bar{\rho} = 0.011$	Mode E $\bar{\varepsilon} = 0.2$ 	Mode F $\bar{\varepsilon} = 0.2$ 
Mode F $l/d = 100$ $\bar{\rho} = 0.0006$	$\bar{\varepsilon} = 0.2$ 	$\bar{\varepsilon} = 0.2$ 

Table 4. Influence of the carburisation depth h/d upon the deformed geometries of a pyramidal lattice made from solid struts $t/d = 0.5$. Results are given for three selected values of l/d .

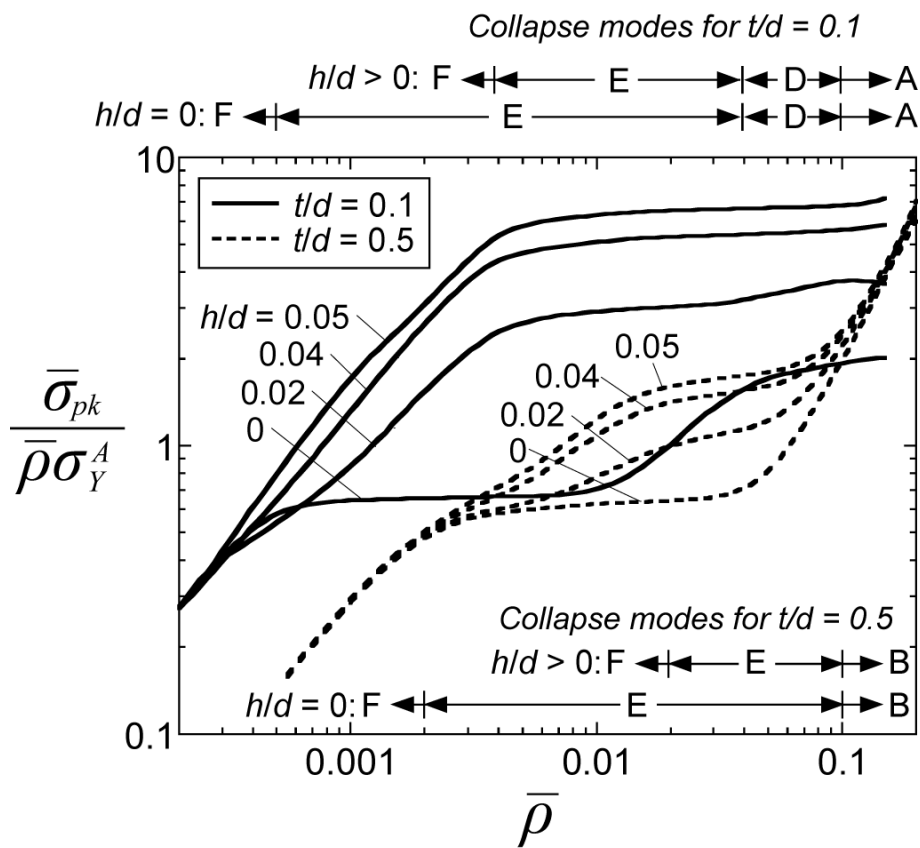


Fig. 13. Influence of the carburation depth h/d upon the normalised compressive strength of a pyramidal lattice made from tubes $t/d = 0.1$ or solid struts $t/d = 0.5$.

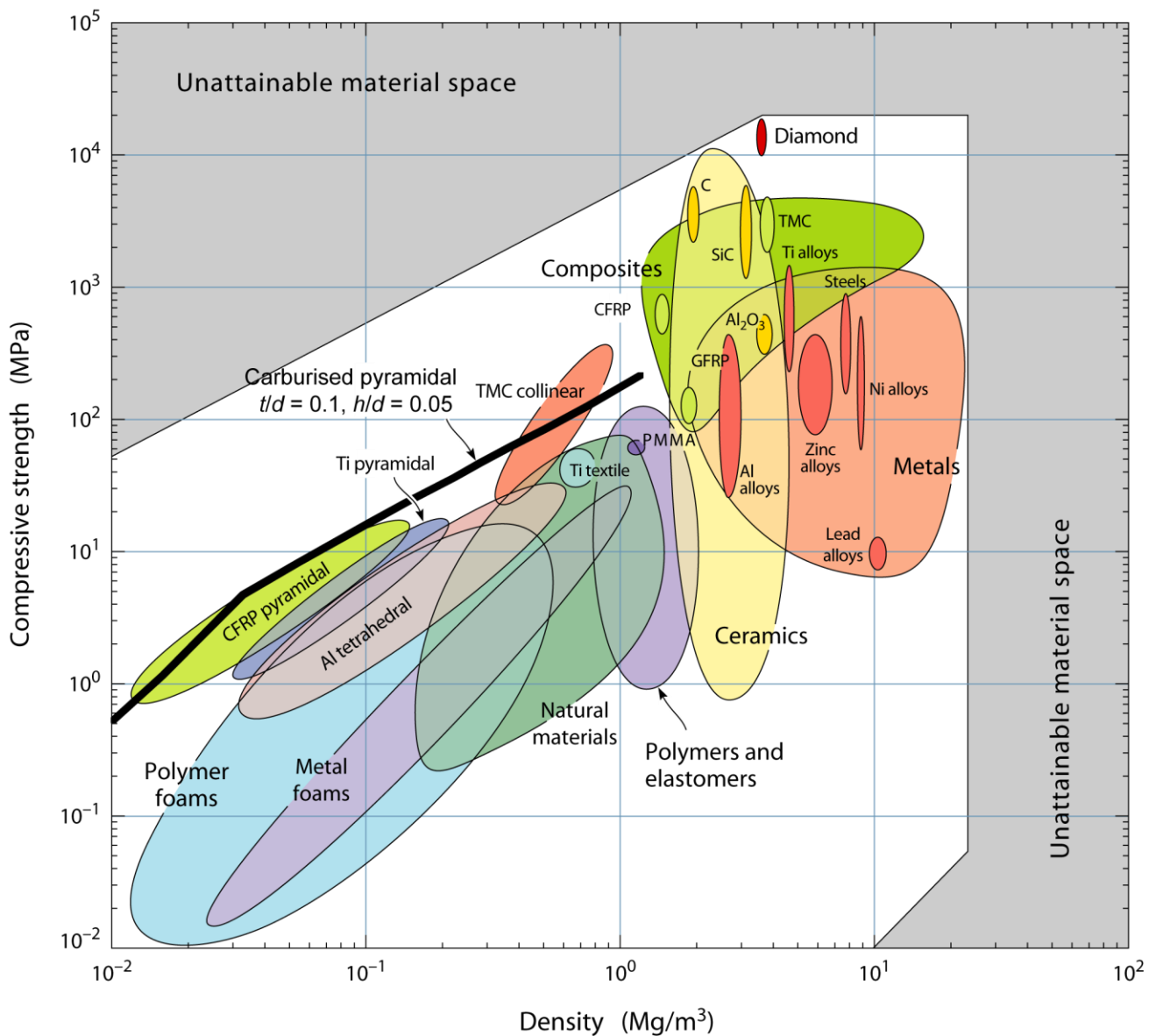


Fig. 14. Material property chart of compressive strength versus density. The predicted compressive strength of a pyramidal lattice made from carburised tubes ($t/d = 0.1$ and $h/d = 0.05$) is also included. Al, aluminium; CRFP, carbon fibre reinforced polymers; Ti, titanium; TMC, titanium matrix composites.

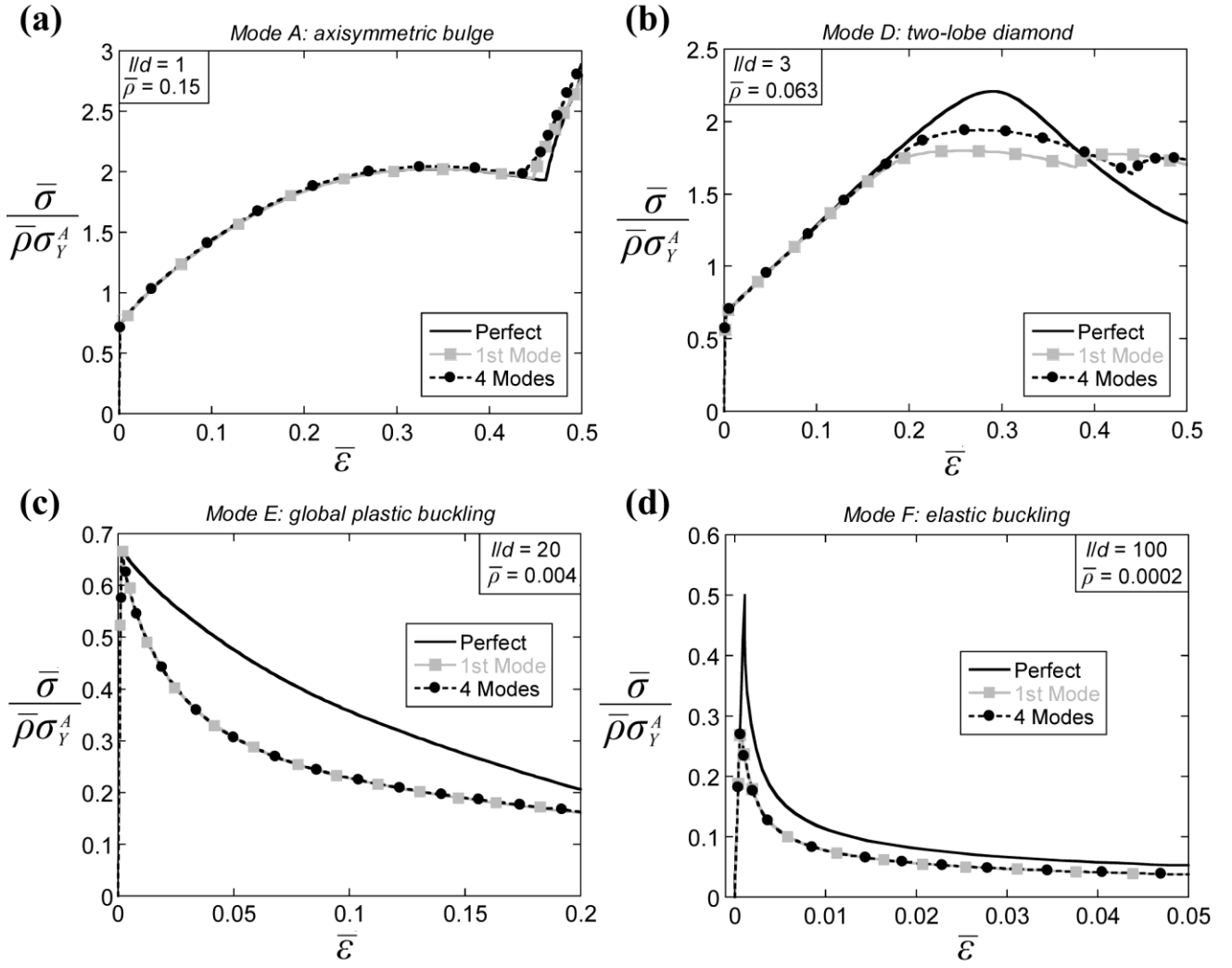


Fig. A.1. Influence of imperfection shape upon the compressive response of a pyramidal lattice made from tubes $t/d = 0.1$. In all cases, the imperfection amplitude is $\zeta = 0.05t$. Results are given for (a) $l/d = 1$, (b) $l/d = 3$, (c) $l/d = 20$ (d) $l/d = 100$.

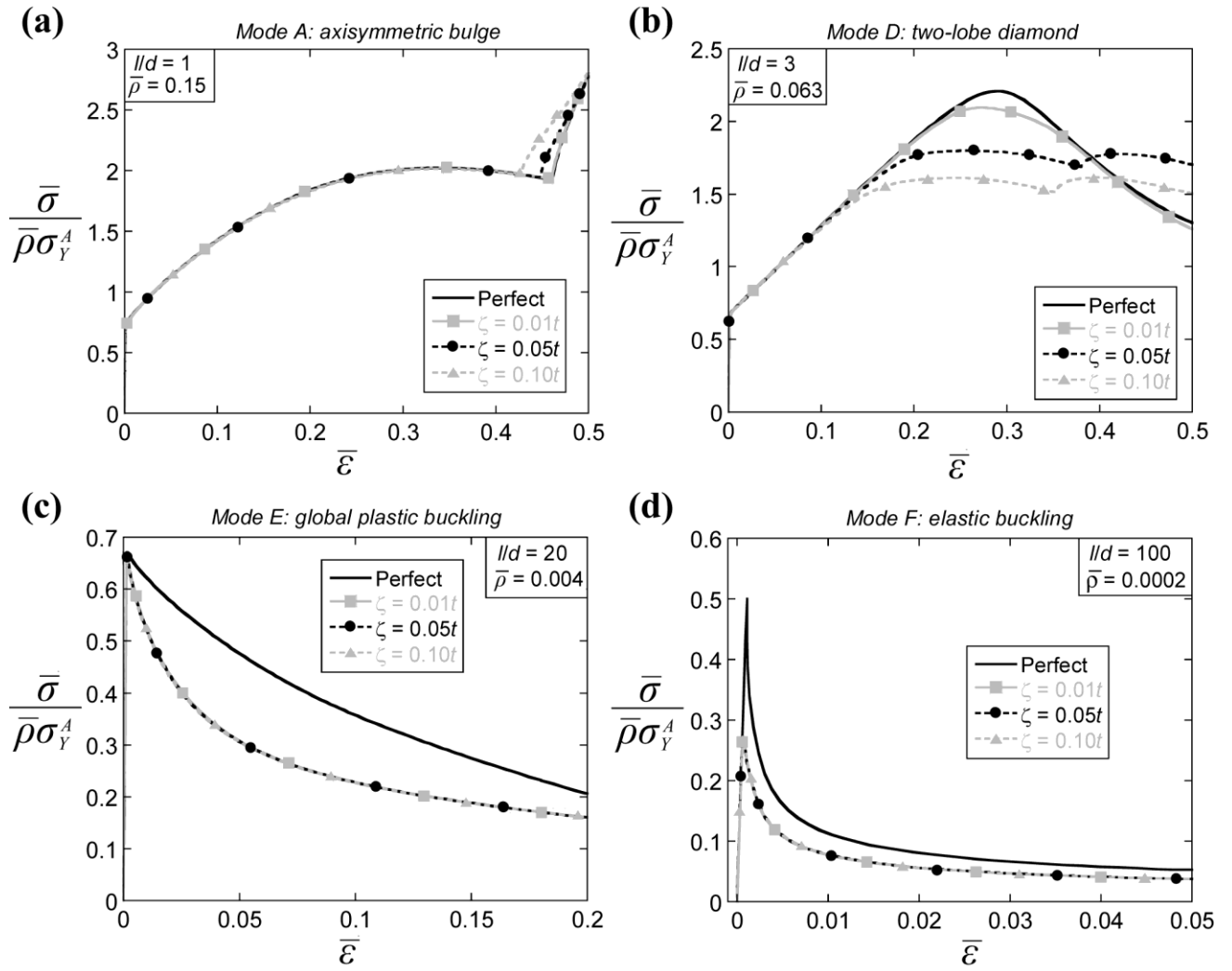


Fig. A.2. Influence of imperfection amplitude upon the compressive response of a pyramidal lattice made from tubes $t/d = 0.1$. In all cases, the imperfection shape is in the form of the first buckling mode. Results are given for (a) $l/d = 1$, (b) $l/d = 3$, (c) $l/d = 20$ (d) $l/d = 100$.

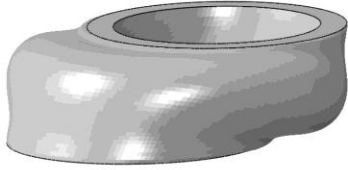
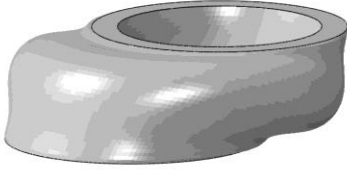
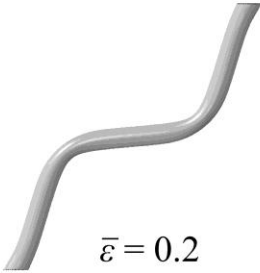
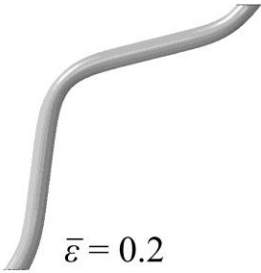
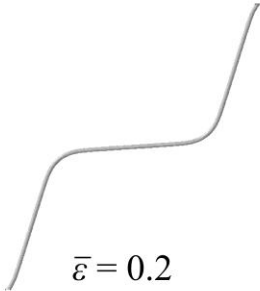
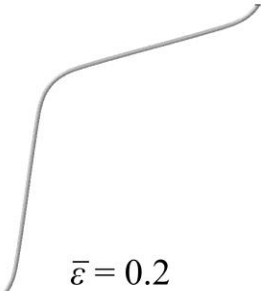
Geometry	Perfect	1st mode $\zeta = 0.05t$
Mode A $l/d = 1$ $\bar{\rho} = 0.15$	 $\bar{\varepsilon} = 0.5$	 $\bar{\varepsilon} = 0.5$
Mode D $l/d = 3$ $\bar{\rho} = 0.064$	 $\bar{\varepsilon} = 0.5$	 $\bar{\varepsilon} = 0.5$
Mode E $l/d = 20$ $\bar{\rho} = 0.004$	 $\bar{\varepsilon} = 0.2$	 $\bar{\varepsilon} = 0.2$
Mode F $l/d = 100$ $\bar{\rho} = 0.0002$	 $\bar{\varepsilon} = 0.2$	 $\bar{\varepsilon} = 0.2$

Table A.1. Influence of a geometric imperfection upon the deformed geometries of a pyramidal lattice made from tubes $t/d = 0.1$. Results are given for four selected values of l/d .